

Central free–free-dominated 880 μm emission in II Zw 40

Hiroyuki Hirashita^{1*}

¹*Institute of Astronomy and Astrophysics, Academia Sinica, P.O. Box 23-141, Taipei 10617, Taiwan*

2011 July 29

ABSTRACT

The central star-forming region in a blue compact dwarf galaxy, II Zw 40, was observed in the 340 GHz (880 μm) band at ~ 5 arcsec (250 pc) resolution with the Submillimetre Array (SMA). A source associated with the central star-forming complex was detected with a flux of 13.6 ± 2.0 mJy. The structure is more extended than the beam in the east–west direction. The SMA 880 μm flux is analyzed by using theoretical models of radio spectral energy distribution along with centimetre interferometric measurements in the literature. We find (i) that the SMA 880 μm flux is dominated (~ 75 per cent) by free–free emission from the central compact star-forming region, and (ii) that the contribution from dust emission to the SMA 880 μm flux is at most 4 ± 2.5 mJy. We also utilize our models to derive the radio–FIR relation of the II Zw 40 centre, suggesting that free–free absorption at low frequencies ($\nu \lesssim$ several GHz; $\lambda \gtrsim$ several cm) and spatial extent of dust affect the radio–FIR relation.

Key words: dust, extinction — galaxies: dwarf — galaxies: evolution — galaxies: individual (II Zw 40) — H II regions — submillimetre: galaxies

1 INTRODUCTION

Blue compact dwarf galaxies (BCDs) generally host compact and ongoing star formation activities in metal-poor and gas-rich environments (Sargent & Searle 1970; van Zee, Skillman, & Salzer 1998). Because both low metallicity and rich gas content indicate an early evolutionary stage, BCDs can be used as nearby laboratories of primeval galaxies which should exist at high redshift. In some BCDs, the most active class of star formation is taking place in super star clusters (SSCs) (Turner, Ho, & Beck 1998; Kobulnicky & Johnson 1999; Johnson & Kobulnicky 2003), which are expected to ‘mimic’ the starburst in high-redshift primeval galaxies.

II Zw 40 is a well studied BCD with a low oxygen abundance, $12 + \log(\text{O}/\text{H}) = 8.13$ (Thuan & Izotov 2005). This galaxy hosts a high star formation activity associated with the SSCs in the centre. At centimetre wavelengths, the central star-forming region in II Zw 40 is compact and optically thick for free–free absorption, and is categorized as a ‘supernebula’ or ‘ultradense H II region’ (Turner, Ho, & Beck 1998; Kobulnicky & Johnson 1999). Such a dense and compact star formation activity is called ‘active’ mode in Hunt et al. (2003) and Hirashita & Hunt (2004). II Zw 40 is also classified as a Wolf-Rayet galaxy: the Wolf-Rayet feature indicates that the typical age of the current starburst is a few Myr (Vacca & Conti 1992). Buckalew, Kobulnicky, & Dufour (2005) derived an age of 2.6 Myr from the $\text{H}\alpha$ and $\text{H}\beta$ equivalent widths. The $\text{Br}\gamma$ equivalent width also shows age $\lesssim 3$ Myr (Vanzi et al. 2008). Stellar spectral synthetic models support young

ages ~ 2 Myr, although there is an underlying old stellar population (Westera et al. 2004).

In order to trace dense ‘embedded’ star-formation activities, optically thin star formation indicators are useful, such as far-infrared (FIR) dust luminosity (e.g. Kennicutt 1998; Inoue, Hirashita, & Kamaya 2000) and radio (thermal plus non-thermal) luminosity (Condon 1992). Indeed, there is a correlation between FIR and radio luminosities in nearby star-forming galaxies (e.g., de Jong et al. 1985; Helou, Soifer, & Rowan-Robinson 1985), which is naturally explained if both luminosities are strongly connected with star formation activities (Völk 1989). However, the studies of radio–FIR relation are biased to objects with FIR detection (e.g. Condon 1992), which means that a significant dust enrichment has already occurred. Therefore, the evolution of radio–FIR relation in young primeval galaxies is not yet clear. The gas density, the magnetic field strength, and the energy density of cosmic ray electrons affect the evolution of radio emission on various time-scales (Helou & Bica 1993; Niklas & Beck 1997; Murphy 2009; Lacki & Thompson 2010), while the dust enrichment plays a role to increase the FIR luminosity (Hirashita & Hunt 2008).

There have been some observational studies on the evolution of radio–FIR relation along the cosmic age. The radio–FIR relation at moderate and high redshifts ($z \lesssim 4$) is broadly similar to that at the local Universe (e.g. Garrett 2002; Gruppioni et al. 2003; Ibar et al. 2008; Murphy 2009; Michałowski, Watson, & Hjorth 2010), although there is also a slight indication of evolution (Vlahakis, Eales, & Dunne 2007; Seymour et al. 2009; Michałowski et al. 2010). The disadvantage of high- z observations is the difficulty in deriving quantities related to galaxy evolution (age, metallicity, etc.) with high accuracy. On the other hand, studies of nearby metal-poor dwarf

* E-mail: hirashita@asiaa.sinica.edu.tw

2 Hirashita

galaxies as ‘laboratories’ of primeval galaxies provide an alternative way to approach the properties of primeval galaxies. Hopkins, Schulte-Ladbeck, & Drozdovsky (2002) and Wu et al. (2008) conclude that the radio–FIR relation of star-forming dwarf galaxies is similar to that of normal galaxies in spite of the difference in metallicity (see also Klein, Weiland, & Brinks 1991), although Cannon et al. (2005, 2006) find a significant deviation from the canonical radio–FIR relation for some individual dwarf galaxies.

In this paper, we do not take a statistical way, but investigate a single object in details. II Zw 40 is suitable for studying radio–FIR emission in a metal-poor young object, since as mentioned above it hosts an extremely young ($\lesssim 3$ Myr) active star formation with a metallicity of $1/4 Z_{\odot}$ (for the solar metallicity, we adopt $12 + \log O/H = 8.69$; Lodders 2003). In order to spot the young star-forming component, a high resolution is necessary. The star-forming region is resolved well at centimetre wavelengths, while there is no information on FIR–submillimetre (submm) dust emission on such a small scale. A submm interferometric observation is desired for the purpose of resolving the dust emission in the star-forming region. Therefore, we observed II Zw 40 by the Submillimetre Array (SMA; Ho, Moran, & Lo 2004), and we report on this observation in this paper. This observation, combined with centimetre radio interferometric data in the literature, will enable us to obtain the radio–FIR emission properties (or radio–FIR relation) in the very young star-forming region with a low metallicity.

This paper is organized as follows. We explain the observations and the data reduction in Section 2, and describe observational results in Section 3. In Section 4, we interpret the results along with the radio data in the literature by using theoretical models. In Section 5, we analyze the contribution from dust emission to the SMA flux. We discuss the radio–FIR relation based on the SMA observation in Section 6. Finally, we conclude in Section 7. The distance to II Zw 40 is assumed to be $D = 10.5$ Mpc ($cz = 789$ km s $^{-1}$ with $H_0 = 75$ km s $^{-1}$ Mpc $^{-1}$). At this distance, 1 arcsec corresponds to 50.9 pc.

2 OBSERVATIONS AND DATA

The SMA observation of II Zw 40 was carried out in the 340 GHz (880 μ m) band on 2010 March 30 in the subcompact configuration. Six antennas were used with projected antenna separations between 9.5 and 25 m. The receivers have two sidebands, the lower and upper sidebands, which covered the frequency ranges from 331.0 to 335.0 GHz, and from 342.9 to 346.9 GHz, respectively. The visibility data were calibrated with the MIR package, with Mars as a flux calibrator (with an adopted flux of 1194 Jy), quasars J0423–013 and J0730–116 as amplitude and phase calibrators, and quasar 3C273 as a band pass calibrator. The calibrated visibility data were imaged and CLEANed with the MIRIAD package. The synthesized beam has a size of FWHM $5.2'' \times 4.4''$ (265 pc \times 224 pc) with a major axis position angle of $\sim 60^\circ$. The beam roughly matches the size of the region of active star formation in the *Hubble Space Telescope* image (Calzetti et al. 2007) and the Very Large Array (VLA) image (Ulvestad, Johnson, & Neff 2007). The largest angular scale sampled by this observation is $19''$.

In order to estimate the contribution of free–free emission to the 880 μ m SMA flux, we use radio data in the literature (Table 1). The single-dish observations measure the fluxes from the entire galaxy, while the interferometric data are sensitive to angular sizes smaller than θ_{\max} . We also adopt the ‘matched beam’ VLA

Table 1. Radio data used in this paper.

ν (GHz)	θ_{\max} ^a (arcsec)	Flux (mJy)	Image ^b	Fit ^c	Ref. ^d
1.4	—	30.0 ± 0.5	S		1
1.5	—	29.9 ± 0.7	S		2
1.5	—	30.5 ± 1.5	S		3
4.8	—	22 ± 3	S		4
5.0	—	22 ± 4	S		1
5.0	10	15 ± 1	I		5
5.0	4	9 ± 1.5	M	✓	5
5.0	—	21.0 ± 1.9	S		2
8.3	7	12 ± 1	I		5
8.3	4	10 ± 1.5	M	✓	5
15	4	14 ± 1.5	I	✓	5
25	—	18 ± 4	S		4

^a The maximum size scale that is well sampled by the interferometric observation.

^b ‘S’, ‘I’, and ‘M’ represent single dish flux, interferometric flux, and matched beam flux, respectively.

^c If the data is used to fit the radio emission models in Section 4, this column is marked with ✓.

^d References. 1) Jaffe, Perola, & Tarengi (1978); 2) Klein et al. (1991); 3) Deeg et al. (1993); 4) Klein, Wielebinski, & Thuan (1984); 5) Beck et al. (2002).

Table 2. FIR and submm data used in this paper.

λ (μ m)	Flux (mJy)	Image ^a	Ref. ^b
60	6610 ± 700	S	1
65	6900 ± 700	S	2
70	5580 ± 280	S	3
90	6600 ± 700	S	2
100	5800 ± 900	S	1
140	3700 ± 700	S	2
160	3400 ± 900	S	2
160	3140 ± 430	S	3
450	400 ± 90	S	1
450	248 ± 81	S	4
850	90 ± 10	S	1
850	98 ± 14	S	4
880	13.6 ± 2.0	I	5

^a ‘S’ and ‘I’ represent single dish flux and interferometric flux, respectively.

^b References. 1) Hunt et al. (2005); 2) Hirashita et al. (2008); 3) Engelbracht et al. (2008); 4) Galliano et al. (2005); 5) this paper.

fluxes obtained with (u, v) data restricted to baselines greater than 20k λ (i.e. sensitive to structures smaller than 4 arcsec) (Beck et al. 2002). These matched fluxes are used to constrain the properties of the central active star formation. The discrepancy between the matched data and the single-dish data is larger at lower frequencies, which implies that the spectral slope is steeper in the diffuse medium than in the central star-forming region.

For the information on dust emission, we also use FIR data in the literature as listed in Table 2, where the fluxes except for our SMA data are all measured by single-dish observations and represent those of the entire galaxy. We only consider the ‘large grain’ component which is in radiative equilibrium with the ambi-

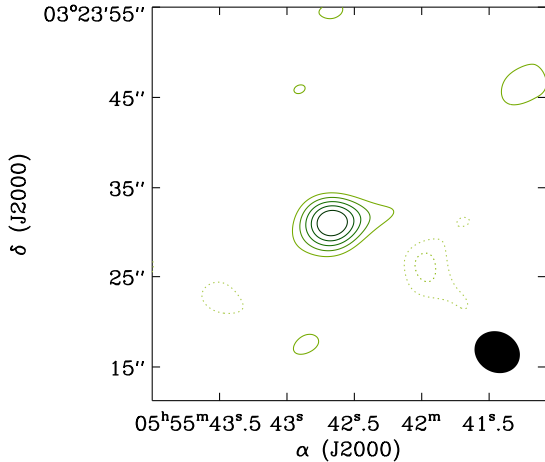


Figure 1. SMA 880 μm continuum image of II Zw 40. Solid contours are 2, 3, 4, 5, and 6 σ ($1 \sigma = 1.15 \text{ mJy beam}^{-1}$), while dotted contours are -2 and -3σ . The beam is shown in the lower right corner.

ent interstellar radiation field (see Section 5.1). Thus, we do not use the data at mid-infrared and shorter wavelengths, where very small grains and PAHs dominate dust emission (e.g. Draine & Li 2001; Dopita et al. 2006) and the spectral energy distribution (SED) is sensitive to grain size distribution.

3 RESULTS

Figure 1 shows the obtained image. The source is clearly detected with a peak intensity of 7.4σ ($1 \sigma = 1.15 \text{ mJy beam}^{-1}$) and a total flux of $13.6 \pm 2.0 \text{ mJy}$. There is an extended feature in the east–west direction with $\text{FWHM} = 7.1 \text{ arcsec}$ (the width of the 2σ contour is $\sim 10 \text{ arcsec}$).

Submm emission in galaxies is usually dominated by dust thermal radiation and contaminated by free–free emission. In order to estimate the contribution from free–free emission, we use the VLA 2 cm continuum data, which is sensitive to spatial scales up to 4 arcsec (Beck et al. 2002). We adopt the emission on this scale as the contribution from the central star-forming region associated with the SSCs. At this wavelength, the single-dish flux is 18.5 mJy , while the VLA flux is $14 \pm 1.5 \text{ mJy}$ (Table 1; Beck et al. 2002); thus, 76 per cent of the total radiation comes from the central star-forming region at 2 cm. Since the emission at 2 cm ($14 \pm 1.5 \text{ mJy}$) is dominated by free–free emission (Beck et al. 2002), we extrapolate the flux to $880 \mu\text{m}$ by assuming a frequency dependence of $\propto \nu^{-0.1}$ (Osterbrock 1989) and estimate the contribution of free–free emission to the $880 \mu\text{m}$ flux to be $10 \pm 1 \text{ mJy}$. Thus, 74_{-10}^{+12} per cent of the flux detected at $880 \mu\text{m}$ by SMA is free-free emission from the central star-forming region. The contribution from free–free emission is further investigated by theoretical models in Section 4. The residual ($4 \pm 2.5 \text{ mJy}$) is possibly dust emission or diffuse (more extended than $4''$ but less than $\sim 10''$) free–free emission.

4 THEORETICAL MODELS

In order to characterize the radio continuum radiation from a star-forming region, thermal free–free radiation from H II regions, non-thermal synchrotron emission from supernova remnants (SNRs), and dust thermal emission should generally be taken into account. Here, we adopt theoretical models for thermal free–free and non-thermal synchrotron components from Hirashita & Hunt (2006) to interpret the emission from the central star-forming region in II Zw 40. Below we briefly summarize their models. We adopt the same values for the physical parameters as those in Hirashita & Hunt (2006) unless otherwise stated. We also add a simple calculation for dust emission in Section 5.

4.1 Basic setups for the star formation

The star formation is assumed to occur in a uniform star-forming region, whose initial number density of hydrogen nuclei is n_{H0} . The mass finally converted into stars, M_0 , is also given. The star formation rate (SFR) as a function of time, $\psi(t)$, is written as $\psi(t) = (\epsilon_{\text{SF}} M_0 / t_{\text{ff}}) e^{-\epsilon_{\text{SF}} t / t_{\text{ff}}}$, where t is the time measured from the onset of the star formation (thus, we assume $\psi = 0$ for $t < 0$), and t_{ff} is the free-fall time-scale estimated by n_{H0} (i.e. the SFR is regulated by the dynamical time-scale; e.g. Elmegreen 2000). We simply introduce an efficiency factor ϵ_{SF} , which means that the gas is converted into stars on a time-scale of $t_{\text{ff}} / \epsilon_{\text{SF}} = 1.4 \times 10^6 (\epsilon_{\text{SF}} / 0.1)^{-1} (n_{\text{H0}} / 10^5 \text{ cm}^{-3})^{-1/2} \text{ yr}$. We treat n_{H0} and M_0 as independent parameters. Throughout this paper, we assume a Salpeter initial mass function (IMF) with a stellar mass range of $0.1\text{--}100 M_{\odot}$.

Since star formation does not proceed on a single free-fall time-scale because of some regulation factors such as magnetic fields, turbulence, radiation, etc. (e.g. Price & Bate 2009), we tentatively adopt $\epsilon_{\text{SF}} = 0.1$ (e.g. Lada, Lombardi, & Alves 2010).¹ Although ϵ_{SF} may be uncertain, the quantities actually constrained by the observational data are the gas mass converted into stars and the gas density (see Section 4.3). As long as these quantities are focused on, the results are insensitive to ϵ_{SF} . Moreover, $t_{\text{ff}} / \epsilon_{\text{SF}}$ is shorter than the lifetimes of massive stars for most of the parameter range in this paper; in this case, the star formation is regarded as instantaneous as long as we consider the evolution at $t \gtrsim t_{\text{ff}} / \epsilon_{\text{SF}}$. If the star formation is instantaneous, total stellar mass M_0 , not the detailed star formation history, determines the total luminosity. Special remarks will be made when we discuss ages too young ($\lesssim 1 \text{ Myr}$) to regard the star formation as instantaneous.

4.2 Radio SED

Thermal free–free radiation is modeled by considering the evolution of the size and density of H II region. In this paper, the recombination coefficient excluding captures to the ground level is assumed to be $\alpha^{(2)} = 1.73 \times 10^{-13} \text{ cm}^3 \text{ s}^{-1}$ (e.g. Spitzer 1978). We assume the density in the H II region to be uniform, and neglect the effects of dust in the H II region. For details on the assumptions, we refer to Hirashita & Hunt (2006).

We consider the time evolution of the hydrogen number density in the H II region, n_{H} , and the radius of the ionized region,

¹ The efficiency factor ϵ_{SF} is different from the star formation efficiency, which is usually defined as the fraction of the finally formed stellar mass to the total initial gas mass. In Lada et al. (2010)’s notation, ϵ_{SF} corresponds to $1/f \sim 0.18$.

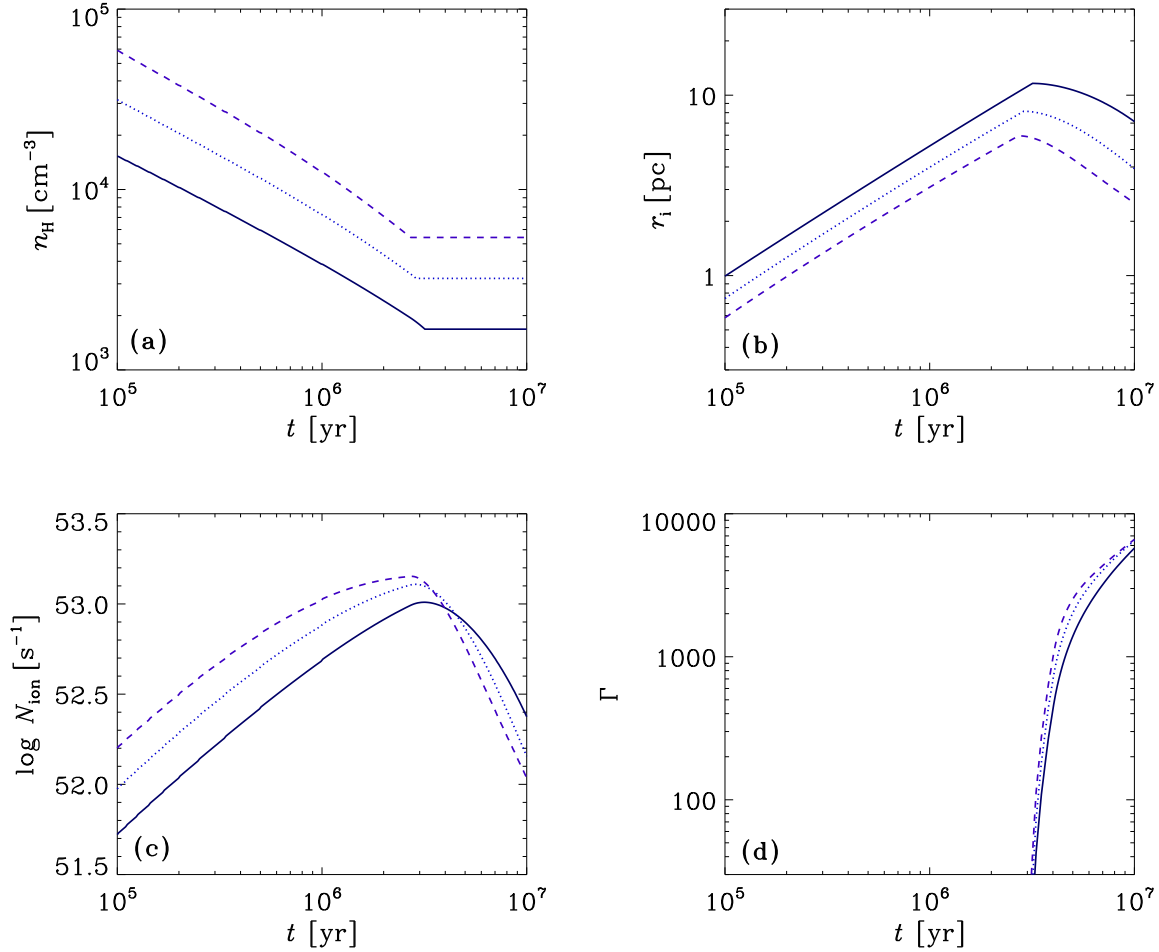


Figure 2. Evolutions of the hydrogen number density n_{H} (Panel a), the ionized radius r_{i} (Panel b), the number of ionizing photons emitted per unit time N_{ion} (Panel c), and the cumulative number of SNe Γ (Panel d). Solid, dotted, and dashed lines are for $n_{\text{H}0} = 3 \times 10^4, 10^5,$ and $3 \times 10^5 \text{ cm}^{-3}$, respectively, with $M_0 = 3 \times 10^6 M_{\odot}$.

r_{i} , according to the evolution of the number of ionizing photons emitted per unit time, N_{ion} . We consider the decrease of n_{H} by pressure-driven expansion, which is assumed to continue until r_{i} starts to decrease by the death of massive stars. In calculating the SED of thermal free-free component, the gas temperature in the H II region is assumed to be $T = 13,000 \text{ K}$ (Thuan & Izotov 2005). We also take free-free absorption into account. In particular, for an H II region in such a dense region as the II Zw 40 centre, free-free absorption is important. The free-free optical depth τ_{ff} is estimated by using the emission measure EM as (Hunt et al. 2004)

$$\tau_{\text{ff}} \simeq 0.328 \left(\frac{T}{10^4 \text{ K}} \right)^{-1.35} \left(\frac{\text{EM}}{10^6 \text{ pc cm}^{-6}} \right) \left(\frac{\nu}{\text{GHz}} \right)^{-2.1}, \quad (1)$$

where EM is estimated in terms of the electron number density n_e and the radius of ionized region r_{i} as $\text{EM} = 4n_e^2 r_{\text{i}}/3$. We assume that the absorbing medium is intermixed with the emitting material; that is, the escape fraction is assumed to be $[1 - \exp(-\tau_{\text{ff}})]/\tau_{\text{ff}}$.

The non-thermal radio luminosity of SNRs is estimated as $L_{\text{nt}}^0(\nu) = l_{\text{nt}} \tau_{\text{nt}}(\nu/5 \text{ GHz})^{-0.5} \gamma(t)$, where $\gamma(t)$ is the rate of

core-collapse supernovae (SNe)² estimated by assuming that stars more massive than $8 M_{\odot}$ become SNe, and $l_{\text{nt}} \tau_{\text{nt}}$ is the radio energy emitted by a SNR over its entire lifetime (fluence) at 5 GHz. The fluence possibly depends on the ambient density (Arbutina & Urošević 2005). We adopt $l_{\text{nt}} \tau_{\text{nt}}(5 \text{ GHz}) = 7.6 \times 10^{22} \text{ W Hz}^{-1} \text{ yr}$, since this value fits the radio SED of SBS 0335–052, which also hosts dense and compact H II regions (Hirashita & Hunt 2006). Free-free absorption is also applied for all the non-thermal component by a screen geometry: i.e. the observed non-thermal luminosity is $L_{\text{nt}} = L_{\text{nt}}^0 e^{-\tau_{\text{ff}}}$. This minimizes the contribution from the non-thermal component especially at low frequencies. If the non-thermal component is not absorbed efficiently, the existence of the non-thermal component is more severely excluded for the II Zw 40 centre (see Section 4.3). Synchrotron self-absorption is not important for SNRs in the frequency range of interest (e.g. Condon 1992).

² In this paper, we only consider core-collapse SNe originating from massive stars.

We also define the cumulative number of SNe, Γ , as

$$\Gamma(t) = \int_0^t \gamma(t') dt'. \quad (2)$$

$\Gamma(t)$ is used as an indicator of the dust production in SNe (Section 5.3).

4.3 Theoretical results for the radio SED

We present the results calculated by the framework described above. We concentrate on the parameter ranges relevant for the central star formation in II Zw 40. As shown later, $n_{\text{H0}} \sim 10^5 \text{ cm}^{-3}$ and $M_0 \sim 3 \times 10^6 M_{\odot}$ fit the radio SED if such a young age $\sim 3 \text{ Myr}$ as indicated by the optical observations (see Introduction) is adopted. The radio luminosity is almost proportional to M_0 , so the constraint on M_0 is rather severe. Thus, we mainly investigate the case of $M_0 = 3 \times 10^6 M_{\odot}$. For the density, we examine $n_{\text{H0}} = 3 \times 10^4, 10^5, \text{ and } 3 \times 10^5 \text{ cm}^{-3}$.

In Fig. 2, we show the key quantities (n_{H} , r_i , N_{ion} , and Γ) as functions of time. The ionized region radius r_i monotonically increases and the density n_{H} decreases until $t \sim 3 \text{ Myr}$ because of the pressure-driven expansion and the increase of N_{ion} . After that, the expansion stops because N_{ion} decreases. The initial SFR is $\psi(0) = \epsilon_{\text{SF}} M_0 / t_{\text{ff}} \simeq 2.2(\epsilon_{\text{SF}}/0.1)(M_0/3 \times 10^6 M_{\odot})(n_{\text{H0}}/3 \times 10^5 \text{ cm}^{-3})^{1/2} M_{\odot} \text{ yr}^{-1}$. The SFR measured by the $\text{H}\alpha$ luminosity is roughly $\sim 1 M_{\odot} \text{ yr}^{-1}$ (van Zee et al. 1998; Vanzi et al. 2008). Since the SFR exponentially decays on a time-scale of $t_{\text{ff}}/\epsilon_{\text{SF}} \sim 1.4(\epsilon_{\text{SF}}/0.1)^{-1}(n_{\text{H0}}/10^5 \text{ cm}^{-3})^{-1/2} \text{ Myr}$ in our models, we obtain the SFR averaged for 3 Myr as $\sim 0.91 M_{\odot} \text{ yr}^{-1}$ ($n_{\text{H0}} = 10^5 \text{ cm}^{-3}$ is assumed), which is near to the value obtained from the $\text{H}\alpha$ line. As shown later, the SFR assumed also reproduces the interferometric radio continuum flux. For the stellar mass, Buckalew, Kobulnicky, & Dufour (2005) derived $6.3 \times 10^6 M_{\odot}$ from a stellar spectral synthesis model (Starburst 99; Leitherer et al. 1999) with a Salpeter IMF of stellar mass range 1–120 M_{\odot} and a metallicity of 1/5 solar. Vanzi et al. (2008) derived $1.7 \times 10^6 M_{\odot}$ with the same spectral synthesis model but with a Kroupa IMF. Our stellar mass ($M_0 \sim 3 \times 10^6 M_{\odot}$) is bracketed by those two results, which means that our stellar mass is consistent with those in the literature within the uncertainty in the IMF. The evolution of Γ is used for the discussion of dust production by SNe in Section 5.3. Γ rapidly increases after $t = 3 \text{ Myr}$, when the first SNe occur.

In Figure 3a, we show the radio SEDs at $t = 1, 3, \text{ and } 5 \text{ Myr}$ with $n_{\text{H0}} = 10^5 \text{ cm}^{-3}$ and $M_0 = 3 \times 10^6 M_{\odot}$. As the age becomes older, the peak shifts to lower frequencies, because the free-free optical depth becomes smaller as the H II region expands. At $t = 1 \text{ and } 3 \text{ Myr}$, the emission is completely dominated by free-free emission, and at $t = 5 \text{ Myr}$, the synchrotron component begins to contribute to the emission and the spectrum slope changes. For comparison, the VLA ‘matched’ data whose (u, v) coverage is restricted to baselines greater than $20 \text{ k}\lambda$ (i.e. sensitive to structures smaller than 4 arcsec) are adopted (three triangles in Fig. 3) as representative fluxes from the central star-forming region.

The density strongly affects the frequency at which the flux peaks because free-free absorption is sensitive to the density. In Fig. 3b, we show the SEDs at $t = 3 \text{ Myr}$ for various initial densities (n_{H0}) with $M_0 = 3 \times 10^6 M_{\odot}$. We observe that the peak position of the SED is indeed sensitive to the density. The rising spectrum of the matched data (triangles) is consistent with free-free absorption.

It is possible to search for the best-fit values of M_0 and n_{H0}

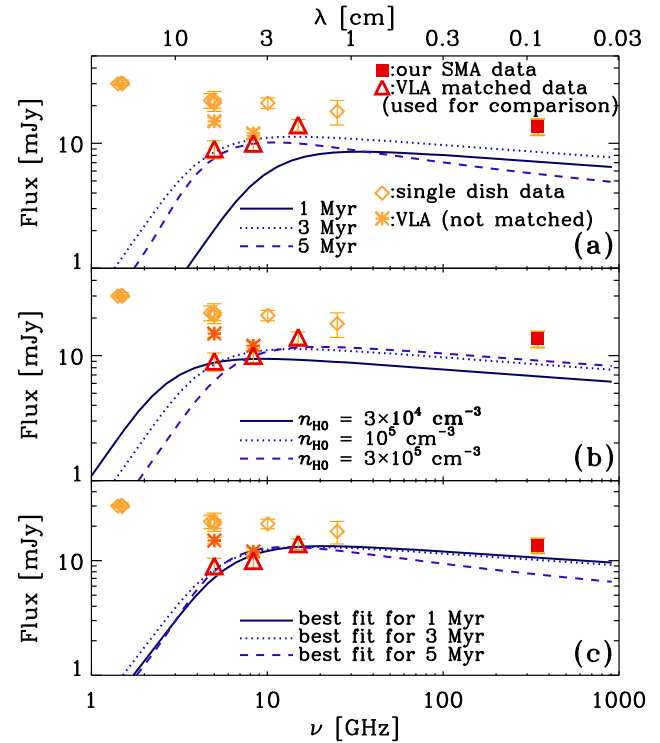


Figure 3. Radio SEDs. (a) Solid, dotted, and dashed lines show the SEDs at 1, 3, and 5 Myr, respectively. The initial hydrogen number density and the total mass converted into stars are fixed with $n_{\text{H0}} = 10^5 \text{ cm}^{-3}$ and $M_0 = 3 \times 10^6 M_{\odot}$, respectively. The observational data (Table 1) are also presented. The filled square represents our SMA measurement at $880 \mu\text{m}$ for the central star-forming region. Diamonds show single-dish measurements by Jaffe et al. (1978), Klein et al. (1984), Klein et al. (1991), while asterisks and triangles indicate the VLA interferometry data by Beck et al. (2002). The triangles at 6, 3.6, and 2 cm are the matched VLA fluxes obtained by restricting (u, v) data to baselines greater than $20 \text{ k}\lambda$ (i.e. sensitive to the structures smaller than 4 arcsec) (Beck et al. 2002). The asterisks at 6 and 3.6 cm are the VLA fluxes synthesized by all the (u, v) data, which are sensitive to structures up to 10 arcsec and 7 arcsec, respectively. (b) Same as Panel (a) but for the SEDs at 3 Myr with various initial densities. Solid, dotted, and dashed lines are for $n_{\text{H0}} = 3 \times 10^4, 10^5, \text{ and } 3 \times 10^5 \text{ cm}^{-3}$, respectively ($n_{\text{H}} = 1.8 \times 10^3, 3.2 \times 10^3, \text{ and } 5.4 \times 10^3 \text{ cm}^{-3}$ at 3 Myr, respectively). (c) Same as Panel (a) but for the best-fit model parameters (M_0 and n_{H0}) listed in Table 3. The fitting is applied for the three triangles (the matched VLA fluxes). The solid, dotted, and dashed lines show the best-fit solutions for $t = 1, 3, \text{ and } 5 \text{ Myr}$, respectively.

for each age. The matched VLA data are adopted (three triangles in Fig. 3) for the χ^2 fitting (one degree of freedom), since our models are applicable to the central star-forming region. The best-fit solutions are shown in Table 3 and Fig. 3c. In the case of $t = 1 \text{ Myr}$, a large M_0 is required since only 29 per cent of M_0 is converted into stars at $t = 1 \text{ Myr}$. As seen in Fig. 3c, the spectral slope at $\nu \gtrsim 15 \text{ GHz}$ for $t = 5 \text{ Myr}$ is different from that at $t \leq 3 \text{ Myr}$ because of the contribution from the non-thermal component. However, the spectral slope at $\nu \gtrsim 15 \text{ GHz}$ in the central part of II Zw 40 is not well constrained because of the lack of the high-resolution data at millimetre wavelengths. For all the three ages, a

Table 3. Best-fit solutions.

Age (Myr)	M_0 (M_\odot)	n_{H0} (cm^{-3})	n_{H} (cm^{-3})	χ^2
1	1.1×10^7 ^a	2.2×10^4	4.7×10^3	2.6
3	3.5×10^6	1.2×10^5	3.7×10^3	2.0
5	4.1×10^6	1.2×10^5	3.9×10^3	2.9

^a Only 29% of M_0 (i.e. $3.2 \times 10^6 M_\odot$) is converted into stars at $t = 1$ Myr.

stellar mass of $\sim 3\text{--}4 \times 10^6 M_\odot$ ³ and a current number density in the H II region of $4\text{--}5 \times 10^3 \text{ cm}^{-3}$ are obtained for the best-fit values.

If the age is about 3 Myr as suggested from the optical and near-infrared observations (Introduction; Vanzi et al. 2008), 75 per cent of the 880 μm flux obtained in our observation is explained by free–free emission according to the best-fit SED at 3 Myr (the flux at 880 μm is 10.2 mJy in the model, while the observed flux is 13.6 mJy). The difference ($\simeq 3.4$ mJy) is likely to be due to the dust and/or diffuse (i.e. not associated with the compact H II region) free–free emission. The dust emission in the central star-forming region is modeled and examined in the next section.

5 CONTRIBUTION FROM DUST IN THE CENTRE

5.1 Dust emission associated with the central star-forming region

Here we model the dust emission associated with the central star-forming region in II Zw 40. We do not model the entire system, so that the following FIR luminosity and dust temperature are valid for the central part of II Zw 40, and are not representative for the global quantities. We consider the wavelength range where large grains, which achieve radiative equilibrium with the ambient stellar radiation field, govern the emission ($\lambda \gtrsim 100 \mu\text{m}$), since the large grains dominate the total dust mass (e.g. Galliano et al. 2005). We do not treat very small grains contributing to mid-infrared emission.

For simplicity, we adopt a shell-like geometry for the dust distribution. This simplification, which is also assumed in Takeuchi et al. (2003, 2005) and Galliano et al. (2005), helps to decrease the number of physical parameters that affect the emergent dust emission SED in relatively minor ways. If the dust is distributed in a thin shell at a distance R_{dust} from the centre, the dust optical depth, τ_{dust} , for the radiation from stars is estimated as

$$\tau_{\text{dust}} = \frac{3M_{\text{dust}}}{16\pi R_{\text{dust}}^2 a s}, \quad (3)$$

where M_{dust} is the total dust mass in the shell, a is the grain radius (uniform spherical grains are assumed), and s is the grain material density. Note that R_{dust} will typically be larger than r_i since the dust associated with surrounding neutral or molecular gas contributes significantly to the FIR luminosity (Xu et al. 1992). In this paper, we adopt $a = 0.1 \mu\text{m}$ and $s = 3 \text{ g cm}^{-3}$ (e.g. Draine & Lee 1984). We estimated the absorption cross section of a grain with the geometrical one because the major heating source is ultraviolet (UV) radiation from OB stars (e.g. Buat & Xu 1996) (i.e. the grain radius is comparable to the wavelength).

³ At $t = 1$ Myr, only 29 per cent of M_0 (i.e. $3.2 \times 10^6 M_\odot$) is converted into stars, while at $t \gtrsim 3$ Myr, most of M_0 is converted into stars (Table 3).

We assume that the UV luminosity is equal to the bolometric luminosity of the OB stars. The OB star luminosity is estimated as a function of time:

$$\mathcal{L}_{\text{OB}}(t) = \int_{3 M_\odot}^{\infty} dm \int_0^{\tau_m} dt' L(m) \phi(m) \psi(t - t'), \quad (4)$$

where $L(m)$ is the main sequence luminosity of a star with mass m and $\phi(m)$ is the IMF. For $L(m)$, we adopt the zero metallicity case in Schaerer (2002) to consider a low-metallicity evolutionary stage, and $L(m)$ may be 2 times smaller if we assume solar metallicity. We assume that the OB stars are located at the centre. This assumption is valid when we consider the central SSCs as the source of UV radiation in II Zw 40. Since the absorbed UV light is reprocessed into FIR wavelengths, the dust FIR luminosity is estimated by

$$\mathcal{L}_{\text{FIR}} = (1 - e^{-\tau_{\text{dust}}}) \mathcal{L}_{\text{OB}}. \quad (5)$$

For simplicity, we adopt a single-temperature approximation for the dust emission, so that the monochromatic luminosity is expressed as

$$L_{\text{FIR}}(\nu) = 4\pi\kappa_\nu M_{\text{dust}} B_\nu(T_{\text{dust}}), \quad (6)$$

where B_ν is the Planck function, κ_ν is the mass absorption coefficient of the dust, and T_{dust} is the dust temperature. We assume that $\kappa_\nu = 0.7(\nu/340 \text{ GHz})^2 \text{ cm}^2 \text{ g}^{-1}$ (James et al. 2002). The dust temperature is determined so that it satisfies the total luminosity constraint:

$$\mathcal{L}_{\text{FIR}} = \int_0^{\infty} L_{\text{FIR}}(\nu) d\nu. \quad (7)$$

By combining Equations (5)–(7), we obtain

$$(1 - e^{-\tau_{\text{dust}}}) \mathcal{L}_{\text{OB}}/M_{\text{dust}} = 1.09 \times 10^{-5} T_{\text{dust}}^6. \quad (8)$$

The dust emission SED, $L_{\text{FIR}}(\nu)$, is determined as follows. R_{dust} is given. Then, a certain test value of M_{dust} is assumed. By using Equation (3), τ_{dust} is obtained. Consequently T_{dust} is derived from Equation (8). Note that the age has to be assumed to evaluate \mathcal{L}_{OB} (Equation 4). Finally, the dust SED $L_{\text{FIR}}(\nu)$ is obtained by Equation (6). If the predicted flux $L_{\text{FIR}}(\nu)/(4\pi D^2)$ overproduces (underproduces) the observed flux, we decrease (increase) M_{dust} and repeat the above procedure.

5.2 Comparison with observational data

As mentioned in Section 4.3, the difference between the predicted flux and the measured one by SMA at 880 μm should be dust emission or diffuse free–free emission. To simplify the discussion, we interpret that all the difference is dust emission, which means that the following values for M_{dust} and L_{FIR} should be taken as upper limits. In the SMA image (Fig. 1), the extension of the 880 μm emission is ~ 10 arcsec. That is, $R_{\text{dust}} \lesssim 250$ pc. Any more extended dust component contributes to the difference between the SMA flux and the SCUBA flux. Also, $R_{\text{dust}} \lesssim 60$ pc is rejected because the dust temperature is so high that the 60 μm flux exceeds the *IRAS* flux. Thus, we investigate $R_{\text{dust}} = 100$ and 250 pc as representative cases. For the free–free component, we adopt the best-fit model for $t = 3$ Myr (Table 3), i.e. $n_{\text{H0}} = 1.2 \times 10^5 \text{ cm}^{-3}$ and $M_0 = 3.5 \times 10^6 M_\odot$ (the dotted line in Figure 3c). For the dust emission, we adopt the dust SED model in Section 5.1, and we adjust M_{dust} so that it reproduces the SMA observational data according to the formulation in Section 5.1: we obtain $(M_{\text{dust}}, T_{\text{dust}}) = (1.8 \times 10^4 M_\odot, 45 \text{ K})$

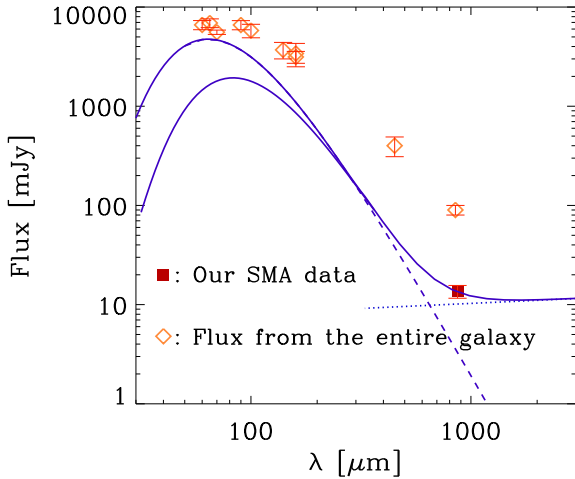


Figure 4. FIR–submm SEDs. Solid, dotted, and dashed lines represent, respectively, the total, the free–free component, and the dust component calculated by the models for the central region in II Zw 40. For the free–free component, the best-fit SED to the matched VLA data for $t = 3$ Myr (i.e. the dotted line in Fig. 3c) is adopted. The dust mass is adjusted to reproduce the SMA data point at $880 \mu\text{m}$ (filled square). Two cases for the radius of dust distribution are examined: $R_{\text{dust}} = 100$ and 250 pc for the upper and lower solid lines, respectively. As upper limits for the flux in the central region, we also show observational data for the entire II Zw 40 system (open diamonds), which are taken from Vader et al. (1993) for 60 and $100 \mu\text{m}$ (*IRAS*), Hunt et al. (2005) for 450 , and $850 \mu\text{m}$ (*SCUBA*), Galliano et al. (2005) for 450 and $850 \mu\text{m}$ (*SCUBA*), Engelbracht et al. (2008) for 70 and $160 \mu\text{m}$ (*Spitzer*), Hirashita et al. (2008) for 65 , 90 , 140 , and $160 \mu\text{m}$ (*AKARI*). The observational data are summarized in Table 2.

and $(2.7 \times 10^4 M_{\odot}, 35 \text{ K})$, for $R_{\text{dust}} = 100$ and 250 pc, respectively. We present the SEDs in Figure 4. As upper limits for the flux from the central part, we also show the data taken by *IRAS* (Vader et al. 1993), *AKARI* (Hirashita et al. 2008), *Spitzer* (Engelbracht et al. 2008) and *SCUBA* (Galliano et al. 2005; Hunt, Bianchi, & Maiolino 2005) for the fluxes from the entire system. Although mid-infrared *Spitzer* data are available with resolutions comparable to our SMA data, mid-infrared emission comes from a different dust component, very small grains, as mentioned in Section 5.1. Thus, we only concentrate on FIR and submm wavelengths where large grains dominate the dust emission.

Fig. 4 shows that a significant fraction of the 60 – $100 \mu\text{m}$ flux (71 per cent of the *IRAS* $60 \mu\text{m}$ flux and 54 per cent of the *IRAS* $100 \mu\text{m}$ flux) is explained by the emission from the central star-forming region for $R_{\text{dust}} = 100$ pc. If we adopt $R_{\text{dust}} = 250$ pc, the contribution from the central star-forming region is smaller (22 per cent of the *IRAS* $60 \mu\text{m}$ flux and 31 per cent of the *IRAS* $100 \mu\text{m}$ flux) because of a lower dust temperature. In any case, an additional emission from a diffuse dust component is necessary to explain the FIR fluxes of the entire system, especially, at wavelengths longer than $100 \mu\text{m}$.

5.3 The origin of dust in the centre

Now we consider the origin of dust in the II Zw 40 centre. One of the natural explanations for the dust mass derived above (~ 2 – $3 \times 10^4 M_{\odot}$) is production in previous episodes of star formation (i.e. preexisting). First, before investigating the possibility of preexisting dust, we examine how much dust

can be produced in the current star formation activity. Because the age is young, SNe are the only source of dust grains and evolved low-mass stars such as asymptotic giant branch (AGB) stars are negligible (Valiante et al. 2009; Gall, Andersen, & Hjorth 2011). Theoretical studies suggest that ~ 0.1 – $1 M_{\odot}$ of dust grains condense in a SN (Kozasa, Hasegawa, & Nomoto 1989; Todini & Ferrara 2001; Nozawa et al. 2003; Bianchi & Schneider 2007; Nozawa et al. 2007, 2010). Infrared and submm observations of SNRs also detected ~ 0.01 – $1 M_{\odot}$ of dust (e.g., Rho et al. 2009; Dunne et al. 2009; Gomez et al. 2009; Matsuura et al. 2011), although quantitative significance of SNe to the dust enrichment in the early galaxy evolution is still debated (Nozawa et al. 2010, and references therein). If we adopt $1 M_{\odot}$ as the ‘maximum’ dust yield per SN, the total dust mass 1 – $3 \times 10^4 M_{\odot}$ is explained only if at least 10^4 SNe occur. (If we consider dust destruction in SNe, more SNe are necessary to explain the total dust amount.) According to Fig. 2, Γ does not reach this number even at $t = 10^7$ yr. Thus, we conclude that the excess at $880 \mu\text{m}$ observed in the centre of II Zw 40, if the emission comes from dust, should be contributed from preexisting dust.

As for the possibility of preexisting dust, we may be observing the preexisting dust itself, or dust grains after the growth by the accretion of metals. Hirashita & Kuo (2011) derive the dust growth time-scale for silicate (a similar time-scale is obtained for carbonaceous dust):

$$\tau_{\text{grow}} \simeq 2.1 \times 10^7 \text{ yr} \left(\frac{\langle a^3 \rangle / \langle a^2 \rangle}{0.1 \mu\text{m}} \right) \left(\frac{Z}{1 Z_{\odot}} \right)^{-1} \times \left(\frac{n_{\text{H}}}{10^3 \text{ cm}^{-3}} \right)^{-1} \left(\frac{T_{\text{gas}}}{50 \text{ K}} \right)^{-1/2} \left(\frac{S}{0.3} \right)^{-1}, \quad (9)$$

where $\langle a^3 \rangle$ and $\langle a^2 \rangle$ are the averages of a^3 and a^2 (a is the grain radius) for grain size distribution, Z is the metallicity, n_{H} is the hydrogen number density, T_{gas} is the gas temperature, and S is the sticking efficiency of the relevant metal species onto the dust surface. We assume $\langle a^3 \rangle / \langle a^2 \rangle = 0.1 \mu\text{m}$, $Z = 1/4 Z_{\odot}$ (see Introduction), $n_{\text{H}} = 10^5 \text{ cm}^{-3}$ (Table 3), $T_{\text{gas}} = 50 \text{ K}$ (Wilson, Walker, & Thornley 1997), and $S = 0.3$ (Leitch-Devlin & Williams 1985; Grassi et al. 2011). Then, we obtain $\tau_{\text{grow}} \sim 8.4 \times 10^5$ yr, which is comparable to the star formation time-scale. Therefore, if the preexisting grains survive before the current star formation episode, they can grow by the accretion of gas-phase metals.

6 RADIO–FIR RELATION

The $880 \mu\text{m}$ emission in the II Zw 40 centre is dominated by free-free emission. At this wavelength, the emission is usually dominated by dust on a galactic scale. Thus, we expect that the properties of FIR dust emission and radio free–free emission in the II Zw 40 centre are different from global galaxy properties. In this section, we examine this expectation quantitatively by using the results in the above sections. Hereafter, we use the term ‘‘FIR luminosity’’ for the dust emission luminosity integrated over 8 – $1000 \mu\text{m}$.

In Fig. 5, we show the relation between the monochromatic luminosity at 1.4 GHz ($L_{1.4 \text{ GHz}}$) and the FIR luminosity L_{FIR} for the central star-forming region in II Zw 40. The radio luminosity at 1.4 GHz is adopted from the best-fit model for $t = 3 \text{ Myr}$ (Figure 3c), while the FIR luminosity is evaluated for $R_{\text{dust}} = 100$ and 250 pc (Section 5.2; Fig. 4). Since all the difference between the model free–free flux and the observed $880 \mu\text{m}$ flux is assumed to

come from dust, the FIR luminosities estimated from the models should be taken as upper limits.

For comparison, we also plot the observational data of BCDs in Fig. 5. The sample is taken from Hopkins et al. (2002) for the FIR and 1.4 GHz luminosities of the entire system (i.e. global luminosities). We only adopt the objects with detections by the NRAO VLA Sky Survey (NVSS) at $\nu = 1.4$ GHz (Condon et al. 1998) and by the *IRAS* at $\lambda = 60$ μm (large open squares). We also adopt the radio flux measured by the Faint Images of the Radio Sky at Twenty cm (FIRST; Becker, White, Helfand 1995) (small open squares). The FIRST flux is systematically smaller than the NVSS flux. The probable reason which Hopkins et al. (2002) suggest is the difference in their sensitivity to extended emission: FIRST images tend to miss extended emission whose angular size is larger than about 2 arcmin. The FIR luminosity of the BCD sample is estimated based on the *IRAS* 60 μm and 100 μm fluxes obtained from NASA/IPAC Extragalactic Database (NED). As an observational estimate of the FIR luminosity L_{FIR} , we adopt an empirically derived formula by Nagata et al. (2002), who estimate the total dust luminosity at $\lambda \geq 40$ μm by using the *IRAS* 60 and 100 μm fluxes. Nagata et al. (2002) take into account the contribution from wavelengths longer than the *IRAS* bands by integrating the modified blackbody spectrum, but they do not consider the contribution from $\lambda < 40$ μm . Therefore, the FIR fluxes may be underestimated by < 30 per cent. However, Nagata et al. (2002)'s method can avoid a significant underestimate in a simple *IRAS* luminosity by Helou et al. (1988), who only considered the contribution from the luminosity in the *IRAS* FIR bands.⁴ If a sample BCD is not detected at 100 μm , we utilize the upper limit at 100 μm to estimate an upper limit of L_{FIR} . The data with upper limits are shown by crosses in Figure 5 ($L_{1.4 \text{ GHz}}$ is taken from the NVSS data). We also show the global luminosities of II Zw 40, whose 1.4 GHz and FIR data are taken from Jaffe et al. (1978) and Vader et al. (1993), respectively.

In order to quantitatively discuss the possible deviation from the standard radio–FIR relation for BCDs, we adopt the radio-to-FIR ratio as usually used (e.g. Condon 1992). Here we define $q_{1.4}$ and q_{15} as

$$q_{1.4} \equiv \log \left(\frac{L_{\text{FIR}}}{3.75 \times 10^{12} \text{ W}} \right) - \log \left(\frac{L_{1.4 \text{ GHz}}}{\text{W Hz}^{-1}} \right), \quad (10)$$

$$q_{15} \equiv \log \left(\frac{L_{\text{FIR}}}{3.75 \times 10^{12} \text{ W}} \right) - \log \left(\frac{L_{15 \text{ GHz}}}{\text{W Hz}^{-1}} \right). \quad (11)$$

The average and the standard deviation of $q_{1.4}$ are calculated for the sample detected by both *IRAS* (60 and 100 μm) and NVSS, while those of q_{15} are determined for the sample in Hunt et al. (2005). The averages of $q_{1.4}$ and q_{15} are 2.39 and 2.89, respectively, and the standard deviations are 0.19 and 0.26, respectively. We also show the lines with $q_{1.4} = 2.39 \pm 0.19$ and $q_{15} = 2.89 \pm 0.26$ to show how much the radio–FIR relation in the central part of II Zw 40 is deviated from the reference radio–FIR relation for the BCDs.

From Fig. 5, we observe that the central region of II Zw 40 has a suppressed 1.4 GHz luminosity and is located below the radio–FIR relation of global BCDs, if the FIR luminosity of II Zw 40 has a value near to the upper limit. This is interpreted to be due to free–free absorption in our models (Fig. 3). Our SMA observation is not sensitive to the possible diffuse synchrotron radiation that would not be affected by free–free absorption. Indeed, the relatively high

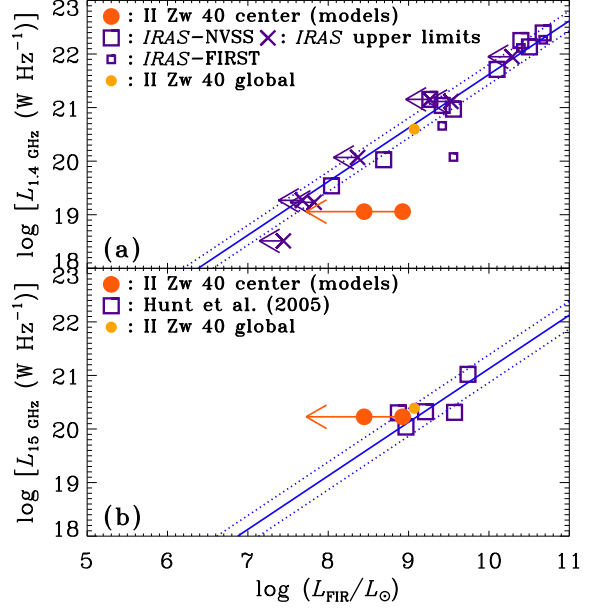


Figure 5. Radio–FIR relation for the central part of II Zw 40 (large filled circles) in terms of the global relations for BCDs. Radio frequencies of 1.4 and 15 GHz are adopted in Panels (a) and (b), respectively. Two cases for the radius of dust distribution are presented for L_{FIR} : $R_{\text{dust}} = 100$ and 250 pc for the right and left points (corresponding the two SEDs in Figure 4). The arrow indicates that the FIR luminosities estimated from the models are taken as upper limits since all the excess over the model free–free emission is assumed to be dust emission. The observational data for the global emission from BCDs in Panel (a) are taken from Hopkins et al. (2002) (large/small open squares are for NVSS/FIRST data and crosses are for non-detection at 100 μm), while those in Panel (b) are taken from Hunt et al. (2005). The entire II Zw 40 system is also plotted (1.4 GHz, 15 GHz, and FIR data are taken from Jaffe et al. 1978, Klein et al. 1991, and Vader et al. 1993, respectively). We also show the lines with $q_{1.4} = 2.39 \pm 0.19$ in Panel (a) and $q_{15} = 2.89 \pm 0.26$ in Panel (b) (solid lines with dotted lines for 1σ) to indicate how much the central part of II Zw 40 is deviated from the reference radio–FIR relation defined for the BCDs.

1.4 GHz flux from the entire galaxy (Fig. 3) indicates the presence of diffuse nonthermal emission in this galaxy. The trend that compact sources have lower radio-to-FIR ratios is also found for luminous infrared galaxies by Condon et al. (1991), who also attribute the lower ratios to free–free absorption.

To avoid free–free absorption, we use the 15 GHz luminosity. The best-fit model for $t = 3$ Myr is used for the 15 GHz luminosity of the II Zw 40 centre (Section 5.2). This luminosity fits the observational data at 15 GHz by Beck et al. (2002). For comparison, we show the global luminosities of BCDs compiled by Hunt et al. (2005) (L_{FIR} is estimated by the method of Nagata et al. 2002; see above). As we observe in Fig. 5b, there is a possibility that the radio–FIR relation is consistent with the global relation if the dust distribution is as compact as $R_{\text{dust}} = 100$ pc (but note that the FIR luminosity is upper limit). If the dust distribution is as extended as $R_{\text{dust}} = 250$ pc, the FIR luminosity is significantly suppressed (or the radio luminosity is enhanced) in the centre of II Zw 40.

The deviation of the II Zw 40 centre in the radio–FIR relation is actually expected, rather than peculiar. Indeed, Cannon et al. (2005) find a spatial variation of FIR-to-radio ratio by an order of magnitude within a metal poor dwarf galaxy, IC 2574.

⁴ For II Zw 40, the global FIR luminosity estimated by Nagata et al. (2002)'s method is $1.2 \times 10^9 L_{\odot}$, while that estimated by Helou et al. (1988)'s method is $9.9 \times 10^8 L_{\odot}$.

Dumas et al. (2011) also show different radio–FIR relations between spiral arms and interarm regions in M51. However, some results show that the radio–FIR correlation holds on 100 pc to sub-kpc scales (Beck & Golla 1988; Xu et al. 1992; Hughes et al. 2006). There are some physical mechanisms that can contribute to the local variation of the radio–FIR relation such as dust processing by SN shocks (Cannon et al. 2005), dust enrichment by the current star formation activity (Hirashita & Hunt 2008), amplification of magnetic fields (Beck & Golla 1988; Dumas et al. 2011), diffusion and escape of cosmic ray electrons (Murphy et al. 2006; Hughes et al. 2006; Murphy et al. 2008), etc. In particular, the diffusion of cosmic ray electrons would predict a large FIR-to-radio ratio on small spatial scales (Hughes et al. 2006). This is not likely to be the reason for the II Zw 40 centre though, as long as its stellar age is too young ($\lesssim 3$ Myr) for SNRs to generate cosmic ray electrons.

If young active star-forming regions generally have similar radio–FIR emission properties to the central part of II Zw 40, free-free dominated submm emission and strong free–free absorption at centimetre and longer wavelengths will be a useful guide to find young active star formation in dense medium. This issue will be further investigated by collecting a sample of active star-forming BCDs with submm interferometry in the future.

7 CONCLUSION

In order to reveal the radiative properties of young active starburst, the central star-forming region in II Zw 40 was observed in the 340 GHz (880 μm) band at $\sim 5''$ resolution with SMA. A source associated with the central star-forming complex was detected with a flux of 13.6 ± 2.0 mJy and a 10-arcsec elongation in the east–west direction. The flux in the central part of II Zw 40 has been analyzed by using the theoretical radio SED model developed by Hirashita & Hunt (2006), and interpreted along with interferometric measurements at centimetre wavelengths in the literature. Then, we have found

(i) that the SMA 880 μm flux is dominated by free-free emission, and

(ii) that possible contribution from dust emission to the SMA flux is less than 4 ± 2.5 mJy.

Our models have been used to derive the radio–FIR relation of the II Zw 40 centre. We have discussed free–free absorption at low frequencies ($\nu \lesssim$ several GHz; $\lambda \gtrsim$ several cm) and spatial distribution of dust (R_{dust}) as possible factors affecting the radio–FIR relation.

ACKNOWLEDGMENTS

We thank Kazushi Sakamoto for his continuous help for the SMA observation and the data analysis and his helpful comments on this paper. We thank the SMA staff for their efforts in running and maintaining the array. We are grateful to the anonymous referee, Takashi Onaka, and the member of our star formation group for useful comments that improved this paper very much. This research has made use of the NASA/IPAC Extragalactic Database (NED), which is operated by the Jet Propulsion Laboratory, California Institute of Technology, under contract with the National Aeronautics and Space Administration. This research is supported through NSC grant 99-2112-M-001-006-MY3.

REFERENCES

- Arbutina, B., & Urošević, D. 2005, *MNRAS*, 360, 76
 Beck, R., & Golla, G. 1988, *A&A*, 191, L9
 Beck, S. C., Turner, J. L., Langland-Shula, L. E., Meier, D. S., Crosthwaite, L. P., & Gorjian, V. 2002, *AJ*, 124, 2516
 Becker, R. H., White, R. L., & Helfand, D. J. 1995, *ApJ*, 450, 559
 Bianchi, S., & Schneider, R. 2007, *MNRAS*, 378, 973
 Buat, V., & Xu, C. 1996, *A&A*, 306, 61
 Buckalew, B. A., Koblunicky, H. A., & Dufour, R. J. 2005, *ApJS*, 157, 30
 Calzetti, D., et al. 2007, *ApJ*, 666, 870
 Cannon, J. M., et al. 2005, *ApJ*, 630, L37
 Cannon, J. M., et al. 2006, *ApJ*, 647, 293
 Condon, J. J. 1992, *ARA&A*, 30, 575
 Condon, J. J., Cotton, W. D., Greisen, E. W., Yin, Q. F., Perley, R. A., Taylor, G. B., Broderick, J. J. 1998, *AJ*, 115, 1693
 Condon, J. J., Huang, Z.-P., Yin, Q. F., & Thuan, T. X. 1991, *ApJ*, 378, 65
 Deeg, H.-J., Brinks, E., Duric, N., Klein, U., & Skillman, E. 1993, *ApJ*, 410, 626
 de Jong, T., Klein, U., Wielebinski, R., & Wunderlich, E. 1985, *A&A*, 147, L6
 Dopita, M. A., et al. 2006, *ApJ*, 639, 788
 Draine, B. T., & Lee, H. M. 1984, *ApJ*, 285, 89
 Draine, B. T., & Li, A. 2001, *ApJ*, 551, 807
 Dumas, G., Schinnerer, E., Tabatabaei, F. S., Beck, R., Velusamy, T., & Murphy, E. 2011, *AJ*, 141, 41
 Dunne, L., et al. 2009, *MNRAS*, 394, 1307
 Elmegreen, B. G. 2000, *ApJ*, 530, 277
 Engelbracht, C. W., Rieke, G. H., Gordon, K. D., Smith, J.-D. T., Werner, M. W., Moustakas, J., Willmer, C. N. A., & Vanzi, L. 2008, *ApJ*, 678, 804
 Gall, C., Andersen, A., & Hjorth, J. 2011, *A&A*, 528, A13
 Galliano, F., Madden, S. C., Jones, A. P., Wilson, C. D., & Bernard, J.-P. 2005, *A&A*, 434, 867
 Garrett, M. A. 2002, *A&A*, 384, L19
 Gomez, H. L., et al. 2009, *MNRAS*, 397, 1621
 Grassi, T., Krstić, P., Merlin, E., Buonomo, U., Piovan, L., & Chiosi, C. 2011, *A&A*, in press
 Gruppioni, C., Pozzi, F., Zamorani, G., Ciliegi, P., Lari, C., Calabrese, E., La Franca, F., & Matute, I. 2003, *MNRAS*, 341, L1
 Helou, G., & Bica, M. D. 1993, *ApJ*, 415, 93
 Helou, G., Khan, I. R., Malek, L., & Boehmer, L. 1988, *ApJS*, 68, 151
 Helou, G., Soifer, B. T., & Rowan-Robinson, M. 1985, *ApJ*, 298, L7
 Hirashita, H., & Hunt, L. K. 2004, *A&A*, 421, 555
 Hirashita, H., & Hunt, L. K. 2006, *A&A*, 460, 67
 Hirashita, H., & Hunt, L. K. 2008, *Mapping the Galaxy and Nearby Galaxies (Ap&SS Proceedings Ser.)*, ed. K. Wada & F. Combes, p. 333
 Hirashita, H., Kaneda, H., Onaka, T., & Suzuki, T. 2008, *PASJ*, 60, S477
 Hirashita, H., & Kuo, T.-M. 2011, *MNRAS*, in press
 Ho, P. T. P., Moran, J. M., & Lo, K. Y. 2004, *ApJL*, 616, L1
 Hopkins, A. M., Schulte-Ladbeck, R. E., & Drozdovsky, I. O. 2002, *AJ*, 124, 862
 Hughes, A., Wong, T., Ekers, R., Staveley-Smith, L., Filipović, M., Maddison, S., Fukui, Y., & Mizuno, N. 2006, *MNRAS*, 370, 363
 Hunt, L. K., Bianchi, S., & Maiolino, R. 2005, *A&A*, 434, 849

- Hunt, L. K., Dyer, K. K., Thuan, T. X., & Ulvestad, J. S. 2004, *ApJ*, 606, 853
- Hunt, L. K., Hirashita, H., Thuan, T. X., Izotov, Y. I., & Vanzi, L. 2003, *Galaxy Evolution: Theory and Observations* (Rev. Mex. Astron. Astrofis. Ser. Conf.), ed. V. Avila-Reese, C. Firmani, C. Frenk, & C. Allen (arXiv:astro-ph/0310865)
- Ibar, E., et al. 2008, *MNRAS*, 386, 953
- Inoue, A. K., Hirashita, H., & Kamaya, H. 2000, *PASJ*, 52, 539
- Jaffe, W. J., Perola, G. C., & Tarengi, M. 1978, *ApJ*, 224, 808
- James, A., Dunne, L., Eales, S., Edmunds, M. G. 2002, *MNRAS*, 335, 753
- Johnson, K. E., & Kobulnicky, H. A. 2003, *ApJ*, 597, 923
- Kennicutt, R. C., Jr. 1998, *ARA&A*, 36, 189
- Klein, U., Weiland, H., & Brinks, E. 1991, *A&A*, 246, 323
- Klein, U., Wielebinski, R., & Thuan, T. X. 1984, *A&A*, 141, 241
- Kobulnicky, H. A., & Johnson, K. E. 1999, *ApJ*, 527, 154
- Kozasa, T., Hasegawa, H., & Nomoto, K. 1989, *ApJ*, 344, 325
- Lacki, B. C., & Thompson, T. A. 2010, *ApJ*, 717, 196
- Lada, C. J., Lombardi, M., & Alves, J. F. 2010, *ApJ*, 724, 687
- Leitch-Devlin, M. A., & Williams, D. A. 1985, *MNRAS*, 213, 295
- Leitherer, C., et al. 1999, *ApJS*, 123, 3
- Lodders, K. 2003, *ApJ*, 591, 1220
- Matsuura, M., et al. 2011, *Science*, in press
- Michałowski, M. J., Watson, D., & Hjorth, J. 2010, *ApJ*, 712, 942
- Murphy, E. J. 2009, *ApJ*, 706, 482
- Murphy, E. J., et al. 2006, *ApJ*, 651, L111
- Murphy, E. J., Helou, G., Kenney, J. D. P., Armus, L., & Braun, R. 2008, *ApJ*, 676, 828
- Nagata, H., Shibai, H., Takeuchi, T. T., & Onaka, T. 2002, *PASJ*, 54, 695
- Niklas, S., & Beck, R. 1997, *A&A*, 320, 54
- Nozawa, T., Kozasa, T., Habe, A., Dwek, E., Umeda, H., Tominaga, N., Maeda, K., & Nomoto, K. 2007, *ApJ*, 666, 955
- Nozawa, T., Kozasa, T., Tominaga, N., Maeda, K., Umeda, H., Nomoto, K., & Krause, O. 2010, *ApJ*, 713, 356
- Nozawa, T., Kozasa, T., Umeda, H., Maeda, K., & Nomoto, K. 2003, *ApJ*, 598, 785
- Osterbrock, D. E. 1989, *Astrophysics of Gaseous Nebulae and Active Galactic Nuclei* (Mill Valley: University Science Books)
- Price, D. J., & Bate, M. R. 2009, *MNRAS*, 398, 33
- Rho, J., Reach, W. T., Tappe, A., Hwang, U., Slavin, J. D., Kozasa, T., & Dunne, L. 2009, *ApJ*, 700, 579
- Sargent, W. L. W., & Searle, L. 1970, *ApJ*, 162, L155
- Schaerer, D. 2002, *A&A*, 382, 28
- Seymour, N., Huynh, M., Dwelly, T., Symeonidis, M., Hopkins, A., M^cHardy, I. M., Page, M. J., & Rieke, G. 2009, *MNRAS*, 398, 1573
- Spitzer, L. 1978, *Physical Processes in the Interstellar Medium* (New York: Wiley)
- Takeuchi, T. T., Hirashita, H., Ishii, T. T., Hunt, L. K., & Ferrara, A. 2003, *MNRAS*, 343, 839
- Takeuchi, T. T., Ishii, T. T., Nozawa, T., Kozasa, T., & Hirashita, H. 2005, *MNRAS*, 362, 592
- Thuan, T. X., & Izotov, Y. I. 2005, *ApJS*, 161, 240
- Todini, P., & Ferrara, A. 2001, *MNRAS*, 325, 726
- Turner, J. L., Ho, P. T. P., & Beck, S. C. 1998, *AJ*, 116, 1212
- Ulvestad, J. S., Johnson, K. E., & Neff, S. G. 2007, *AJ*, 133, 1868
- Vacca, W. D., & Conti, P. S. 1992, *ApJ*, 401, 543
- Vader, J. P., Frogel, J. A., Terndrup, D. M., & Heisler, C. A. 1993, *AJ*, 106, 1743
- Valiante, R., Schneider, R., Bianchi, S., & Andersen, A. C. 2009, *MNRAS*, 397, 1661
- van Zee, L., Skillman, E. D., & Salzer, J. J. 1998, *AJ*, 116, 1186
- Vanzi, L., Cresci, G., Telles, E., & Melnick, J. 2008, *A&A*, 486, 393
- Vlahakis, C., Eales, S., & Dunne, L. 2007, *MNRAS*, 379, 1042
- Völk, H. J. 1989, *A&A*, 218, 67
- Westera, P., Cuisinier, F., Telles, E., & Kehrig, C. 2004, *A&A*, 423, 133
- Wilson, C. D., Walker, C. E., & Thornley, M. D. 1997, *ApJ*, 483, 210
- Wu, Y., Charmandaris, V., Houck, J. R., Bernard-Salas, J., Lebouteiller, V., Brandl, B. R., & Farrah, D. 2008, *ApJ*, 676, 970
- Xu, C., Klein, U., Meinert, D., Wielebinski, R., & Haynes, R. F. 1992, *A&A*, 257, 47

This paper has been typeset from a $\text{\TeX}/\text{\LaTeX}$ file prepared by the author.